

Manuscript version: Author's Accepted Manuscript

The version presented in WRAP is the author's accepted manuscript and may differ from the published version or Version of Record.

Persistent WRAP URL:

<http://wrap.warwick.ac.uk/160187>

How to cite:

Please refer to published version for the most recent bibliographic citation information. If a published version is known of, the repository item page linked to above, will contain details on accessing it.

Copyright and reuse:

The Warwick Research Archive Portal (WRAP) makes this work by researchers of the University of Warwick available open access under the following conditions.

© 2021 Elsevier. Licensed under the Creative Commons Attribution-NonCommercial-NoDerivatives 4.0 International <http://creativecommons.org/licenses/by-nc-nd/4.0/>.



Publisher's statement:

Please refer to the repository item page, publisher's statement section, for further information.

For more information, please contact the WRAP Team at: wrap@warwick.ac.uk.

Mechanisms of tripartite permeability evolution for supercritical CO₂ in propped shale fractures

Lei Hou ^{a,*}, Derek Elsworth ^b

^a School of Engineering, The University of Warwick, Coventry CV4 7AL, UK

^b Energy and Mineral Engineering & Geosciences, EMS Energy Institute and G3 Center, Pennsylvania State University, University Park, 16802, USA

Abstract

Characterization of CO₂ flow in propped fractures is important in defining the response to CO₂ injection for reservoir stimulation and CO₂ sequestration. We measure the evolution of permeability in propped fractures of shale to both adsorbing CO₂ and non-adsorbing He under sub- and supercritical conditions. A tripartite permeability-pressure evolution curve is obtained when supercritical, consisting of a dual-U-shaped evolution first below and then exceeding critical pressure with a V-shaped fluctuation spanning the phase transition. The increasing adsorbed-phase-density and resultant swelling stress may control the permeability variation around the critical point. The inorganic adsorbent (mainly clay) may contribute to the secondary U-shaped evolution according to its sorption isotherm. The secondary adsorption may be generated by increasing sorption sites (competitive adsorption between CO₂ and H₂O) or through multi-layered sorption and stronger diffusion of supercritical CO₂. Further constraint is applied through observations of permeability recovery between initial and repeat saturations to non-adsorptive He. An abnormal increment of permeability recovery ratio is obtained for secondary adsorption, which may be caused by the dehydration and shrinkage of the matrix and the dissolution of minerals. Mechanisms of permeability evolution for CO₂ in shale are classified between organic and inorganic fractions. The contributions of adsorption to the permeability evolution are quantified by comparisons for permeation by CH₄ and He. A flat X-shaped trend is apparent, in which the inorganic contribution to permeability increases with increasing pressure while the organic contribution to permeability decreases with increasing pressure. The ratio of inorganic contribution reaches 60–70% under supercritical conditions.

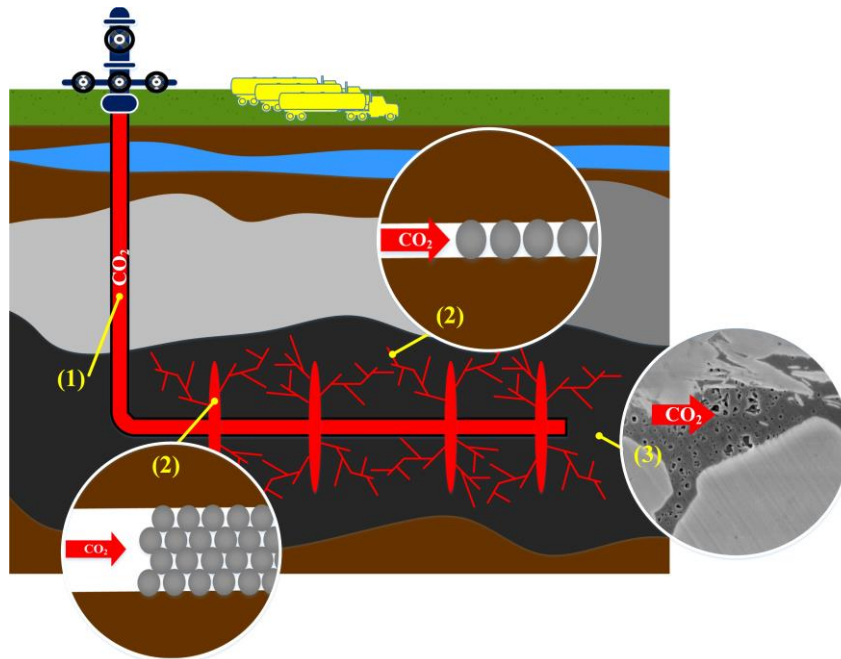
Keywords: propped shale fracture, adsorption, permeability, clay, supercritical CO₂

* Corresponding author.

E-mail address: lei.hou@warwick.ac.uk (L. Hou)

30 1 Introduction

31 CO₂ injection in reservoirs (oil, gas or coal) is a promising approach for both enhancing the
32 recovery of native hydrocarbons and for sequestering carbon emissions. These techniques include
33 CO₂ flooding (Cao & Gu, 2013), fracturing (Hou et al., 2017), replacement (Lan et al., 2019) and
34 storage in saline aquifers or depleted reservoirs (Bielicki et al., 2018; Buscheck, White, Carroll,
35 Bielicki, & Aines, 2016). A typical flow path of CO₂ in a reservoir is shown in Fig. 1, where CO₂
36 flows in through a well (1), then propped fractures (2) and finally into the porous medium (3). This
37 injection may exert significant impacts on the stimulated reservoir volume (SRV) for hydrocarbon (oil
38 and gas) recovery and sealing behaviour for carbon (CO₂) sequestration (Middleton et al., 2015;
39 Tayari & Blumsack, 2020).



40
41 **Fig. 1. Schematic of CO₂ injection in a shale reservoir through (1) a well, (2) propped fractures (main and**
42 **branching fractures) and (3) the porous medium.**

43 Abundant work has examined CO₂ flows in porous media to define interactions between gas and
44 matrix and the corresponding effect on both permeabilities (Ao, Lu, Tang, Chen, & Li, 2017; Zhou et
45 al., 2016; Zhou et al., 2020) and the mechanical properties of rock (Yin, Zhou, Jiang, Xian, & Liu,
46 2016; Yin et al., 2017). Less clarity is available for CO₂ flow in propped fractures, where additional
47 complexity is added with grain-fracture interactions to CO₂. Previous work has focussed on grain-
48 fracture interactions to evaluate permeability loss by embedment under various conditions of closure

49 stress, mineral composition, reservoir temperature and fracturing fluids (Arshadi, Zolfaghari, Piri, Al-
50 Muntasheri, & Sayed, 2017; Kewen Li, 2015; Tang & Ranjith, 2018). Impacts of CO₂-matrix
51 interaction (such as swelling) are relatively less prominent, especially for shales because of their
52 lower organic contents. However, recent studies in high-organic-content Green River shale indicates
53 that swelling could consume as much as 50% of the permeability and increase embedment by a factor
54 of ~2 (Hou, Elsworth, & Geng, 2020).

55 The measurement of permeability is one principal methodology characterizing the evolution of
56 CO₂ fracture flow, which reflects the effects of both swelling and embedment (S. Wang, Elsworth, &
57 Liu, 2011, 2013). A sorbing permeant (CO₂, CH₄ or N₂) swells the rock matrix and forms a typical U-
58 shaped curve for permeability evolution with pressure due to the competition between adsorption and
59 effective stress (Kumar, Elsworth, Liu, Pone, & Mathews, 2015; X. Li et al., 2017). Nonetheless, the
60 underlying mechanisms of adsorption-permeability response for CO₂ permeation in propped fractures
61 remain unclear, due to a variety of factors, including:

62 (1) Clues to the behaviour may be found in the response to CO₂ adsorption, although the common
63 use of powdered rocks rather than the intact samples (Klewiah, Berawala, Alexander Walker,
64 Andersen, & Nadeau, 2020) limits the applicability of observations to fracture flow. The cubic
65 dependence of permeability on fracture aperture magnifies the effect of swelling, thus leading to the
66 appearance that the swelling of a trace content of organics may significantly impact permeability. A
67 similar response is reported in the study of CO₂-clay interactions, where the stiffness of an intact
68 sample may develop higher swelling stress than pure clay could under the same conditions (Zhang, de
69 Jong, Spiers, Busch, & Wentinck, 2018).

70 (2) Swelling of clay minerals is another controlling mechanism. An increasing number of studies
71 reveal a strong positive correlation of shale clay content to sorption capacity of CO₂ (Chalmers &
72 Bustin, 2008; M. Gasparik et al., 2012; Luo et al., 2015; L. Wang & Yu, 2016). CO₂ sorption capacity
73 of powdered montmorillonite is comparable to that of coal (Romanov, 2013). However, excess
74 exposure to supercritical CO₂ may conversely lead to shrinkage of clay by interlayer dehydration
75 (Akono et al., 2019; Lu et al., 2016; Pan & Connell, 2007). More experiments are needed to constrain
76 the effect of such swelling-shrinking response on permeability evolution.

77 (3) The CO₂ phase transition is observed to dramatically change permeability in simple powders
78 (Jia, Tsau, & Barati, 2018), intact coal (Zhi, Elsworth, & Liu, 2019) and propped fractures in shale
79 (Hou et al., 2020; X. Li et al., 2017). A sudden increase in density and kinetic energy may enhance the
80 sorption capacity and plasticize the solid material to generate a precipitous drop in permeability
81 around the critical point. However, more studies are required to constrain this permeability evolution
82 under higher injection pressures where the CO₂ is in a supercritical state and for longer exposure.

83 Towards resolving these impacts, we explore CO₂-shale interactions across the sub- to super-
84 critical phase transition in artificial (proxy-fluid-driven) fractures. We measure permeability evolution
85 with the injection of both non-adsorptive helium (He) and adsorptive carbon dioxide (CO₂) on
86 samples of Green River shale to (i) fully reveal the interaction process from sub- to super-critical
87 pressure, (ii) define the different controlling mechanisms for permeability evolution in different stages
88 of gas injection, and (iii) quantitatively analyze the contributions of each mechanism to provide a
89 mechanistic understanding of characteristics of CO₂ fracture-flow towards improving the practice of
90 oil/gas production and CO₂ sequestration.

91 **2 Methodology**

92 We measure permeability evolution to CO₂ and He in propped fractures in shale *via* pressure
93 transient (pulse) methods. The apparatus (core holder and reservoirs) is immersed within a
94 temperature-controlled water bath to control the state of CO₂, as either sub- or super-critical. We
95 measure permeability to CO₂ and He alternately in the same sample to reveal the influence of
96 adsorption and desorption behaviour.

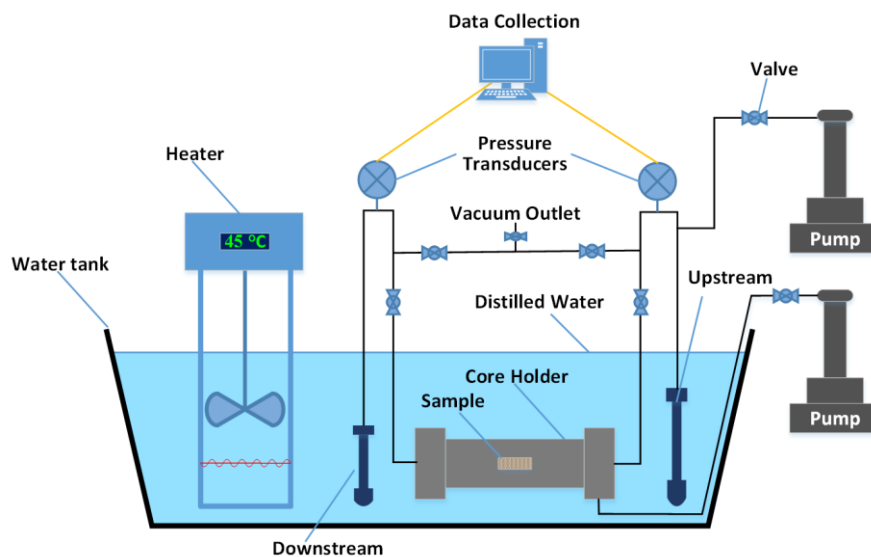
97 **2.1 Materials and preparation**

98 Axially-split core samples (25mm diameter 50mm length) of Green River shale are packed with
99 tape then placed in a pressurized core holder with monolayer proppant (40/80 mesh, Carbo-Lite
100 ceramic proppant) sandwiched within the fracture. We explore the behaviour of a monolayer since the
101 branch fractures or micro-fractures (usually monolayer-propped) compose a crucial component of the
102 total stimulated reservoir volume (Gale, Laubach, Olson, Eichhuble, & Fall, 2014; Hoek & Martin,
103 2014; Weng, 2015). Besides, similar permeating behaviour of CO₂ has been observed for both multi-

104 and mono-layer propped samples, in which the monolayered sample exhibits an amplified swelling
105 effect (X. Li et al., 2017). We use sorbing CO₂ (purity of 99.995 %) and effectively- non-sorbing He
106 (99.999 %) as contrasting permeants for the permeability measurements.

107 2.2 Apparatus

108 A standard triaxial apparatus, as shown in Fig. 2, is used as the pressurized core holder (Temco).
109 Both confining and axial stresses to 25 MPa are applied by syringe pumps (ISCO 500D) to a
110 resolution of ± 0.007 MPa. A Viton rubber jacket is applied to seal and isolate the sample from the
111 confining fluid in the core holder. Reservoir volumes are 26.7 ml for the upstream and 16.8 ml for the
112 downstream with reservoir pressures measured by transducers (Omega PX302-2KGV and Omega
113 PX302-5KGV) to resolutions of ± 0.03 MPa. Each transducer is calibrated for each new sample with
114 National Instruments Labview used for data acquisition and pump control. The tests are performed at
115 both room temperature (23°C) and supercritical temperature (45°C for a supercritical transition at
116 31°C) in a water bath with the core holder and reservoirs immersed, as shown in Fig. 2. Interior gas
117 pressures in the range 2 to 13 MPa access the various phase states of CO₂.



118
119 **Fig. 2. Schematic of the experimental apparatus and water bath system (Hou et al., 2020; S. Wang et al., 2011).**

120 2.3 Procedure

121 We use standard pressure transient (pulse) methods for permeability measurements. A pressure
122 difference (pulse) is applied between upstream and downstream and its upstream decay and

123 downstream build-up behaviour is recorded and analysed to obtain the permeability that is calculated
 124 as (Brace, Walsh, & Frangos, 1968),

$$125 \quad k = \frac{\alpha \mu \beta L V_{up} V_{dn}}{A(V_{up} + V_{dn})} \quad (1)$$

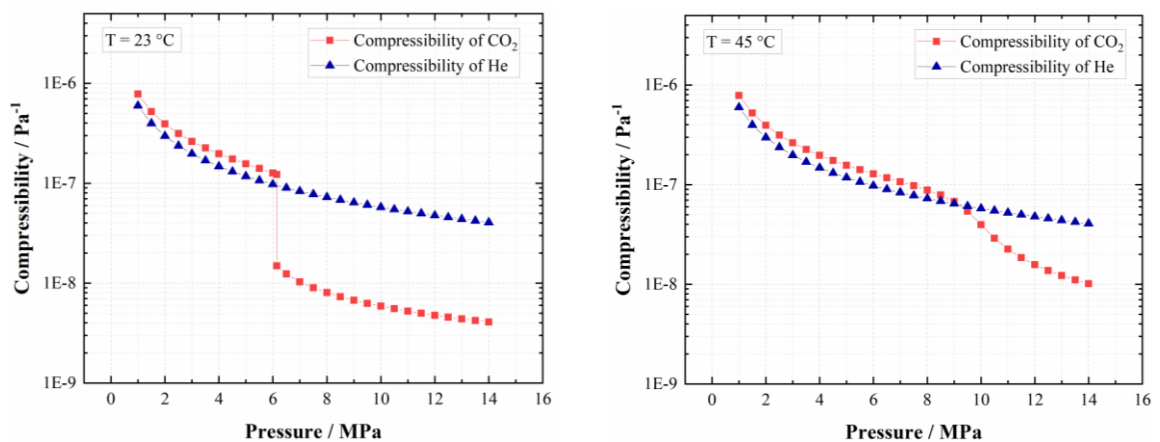
126 where α is the slope of pressure decay against the logarithm of time; μ and β are the viscosity and
 127 compressibility of the fluid, respectively; L is the length of the sample; V_{up} and V_{dn} are volumes of the
 128 upstream and downstream reservoirs, respectively; and A is the fluid flow cross-sectional area in
 129 fracture (permeation through the rock matrix is ignored).

130 The compressibility of the fluid β is calculated from the bulk modulus

$$131 \quad \beta = \frac{1}{B_M} = \frac{1}{v^2 \rho} \quad (2)$$

132 where B_M is the bulk modulus of the fluid; v is the speed of sound in the fluid; ρ is the fluid density.

133 The values of v and ρ are recovered from standard characterizations (National Institute of Standards
 134 and Technology (NIST)). The values of compressibility are calculated and plotted in Fig. 3.



135
 136 **Fig. 3. Compressibility of CO₂ and He (based on NIST database).**

137 **3 Results**

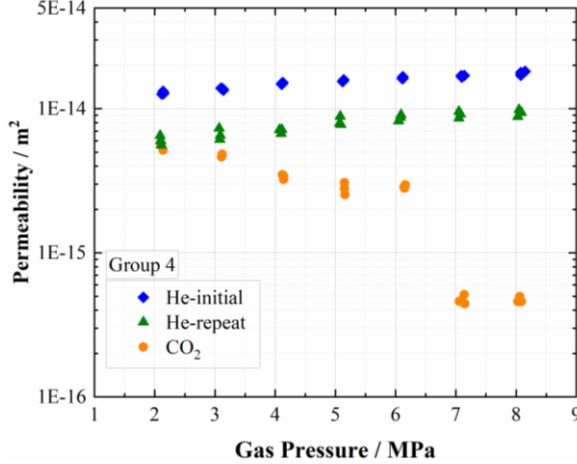
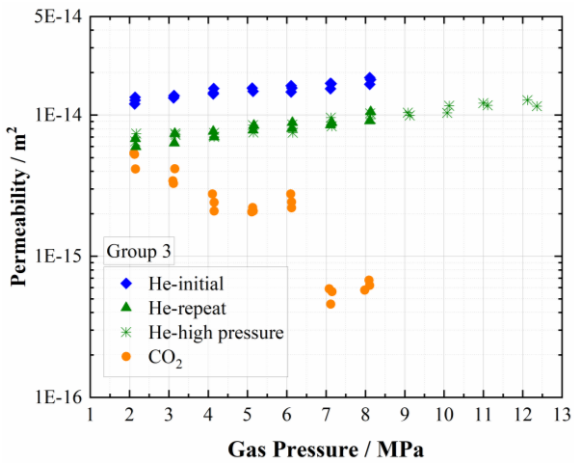
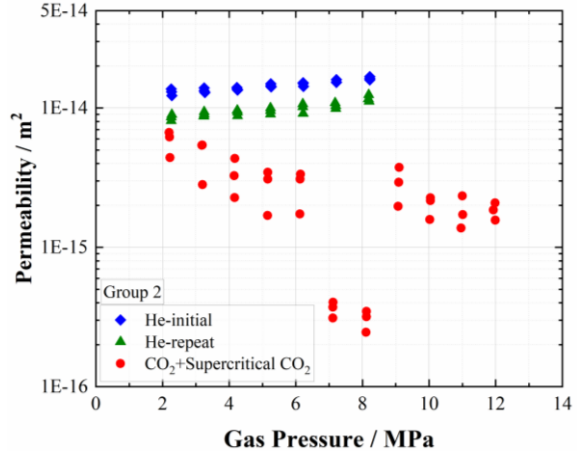
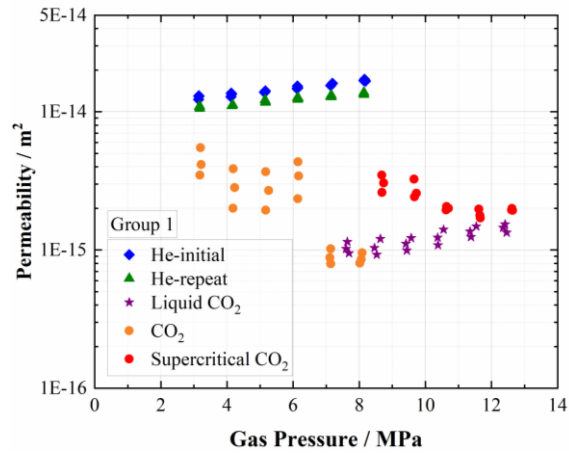
138 Four groups of permeability measurements are conducted and summarized in Table 1. Five rounds
 139 of experiments are carried out in Group 1 for He and CO₂ as gaseous, liquid then supercritical state.
 140 The first four rounds are completed at room temperature (23°C) with the final performed at a
 141 temperature of 45°C beginning at a supercritical pressure. In particular, the permeability to non-
 142 sorbing He is repetitively measured in the same sample before and after the permeation of CO₂ to
 143 compare the impact of CO₂ adsorption and desorption. Each round of experiments involved in Group

144 2 is conducted continuously at 45 °C. Control Group 3 and 4 repeat sub- and super-critical pressure
 145 measurements with non-sorbing He.

146 **Table 1. Matrix of experiments defining samples and conditions.**

Sample Type	Green River Shale			
Group No.	Experimental Group 1	Experimental Group 2	Control Group 3	Control Group 4
Injection Pressure	3 ~ 13 MPa	2 ~ 12 MPa	2 ~ 13 MPa	2 ~ 9 MPa
Temperature	23 °C & 45 °C	45 °C	23 °C	23 °C
CO₂ Phases	Gaseous, Liquid & Supercritical	Supercritical	Gaseous	Gaseous
Dimensions	25 (dia.) * 50 (length) mm			
Proppant	Carbo-Lite Ceramisite (40/80 Mesh)			
Gas	Helium & Carbon Dioxide			
Triaxial Pressure	25 MPa			

147 Observations recovered by probing with both injection (increasing gas pressure) then depletion
 148 (decreasing gas pressure) are plotted in Fig. 4. Generally, positive parallel linear relationships are
 149 recovered between increasing gas pressure and increasing permeability for all cases of He and liquid
 150 CO₂, indicating that deformations under changes in effective stress (confining pressure minuses
 151 injection pressure) dominate the permeability evolution. This is expected for non-adsorptive He since
 152 swelling is absent. For liquid CO₂, with permeability one order-of-magnitude lower than that for He, a
 153 swelling effect may be manifest but is counteracted by the high injection pressure.



154

155

156 **Fig. 4. Permeability evolution versus gas pressure in propped fractures in Green River shale. The repeat He tests are**
 157 **performed after all CO₂ tests in the same sample of each group. Group 2 is completed at 45°C. Group 3 and 4 are at**
 158 **23°C. Group 1 is conducted at both temperatures and for various CO₂ phases.**

159

For the remainder of the CO₂ cases, typical U-shaped curves are observed under subcritical

160

pressures as the result of the competition between adsorption and effective stress. A new U-shaped

161

curve under high pressure is formed for the supercritical CO₂ cases. Results from all CO₂ cases are

162

averaged and presented in Fig. 5. A tripartite permeating behaviour is apparent, consisting of (I) a

163

typical U-shaped curve below the critical pressure, (II) a V-shaped fluctuation around the phase

164

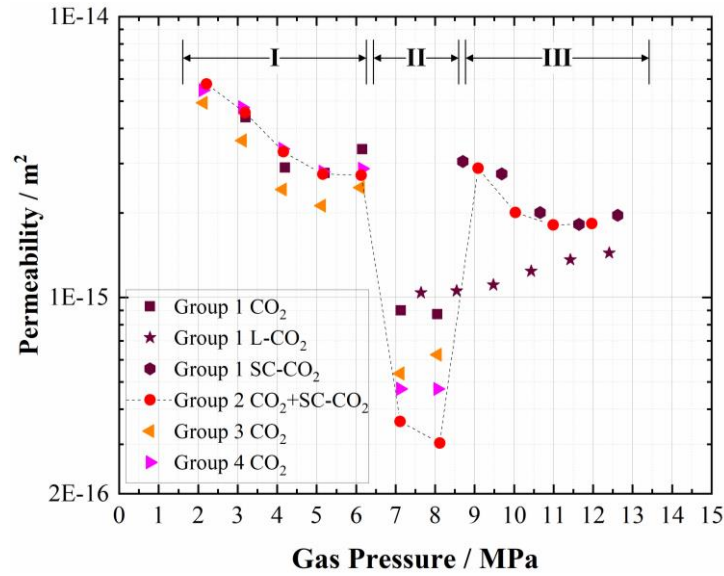
transition point and (III) a secondary U-shaped curve above supercritical pressure and temperature.

165

Part III exhibits a similar parabolic trend as Part I, and reaches the minimum value around a pressure

166

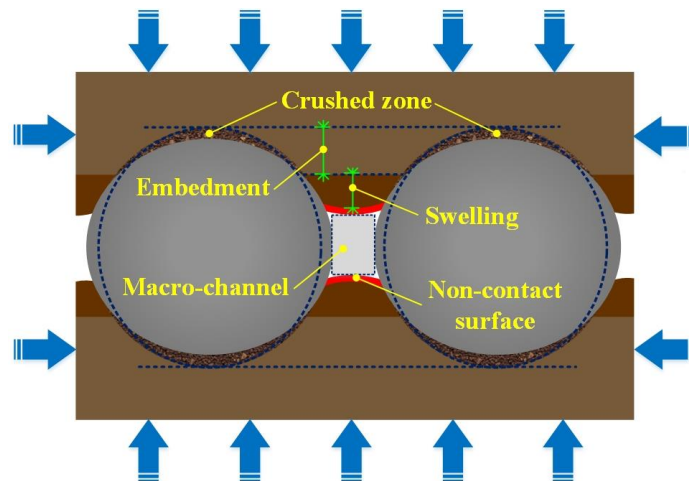
of 11–12 MPa.



167
168 **Fig. 5. Permeability evolution versus gas pressure for all CO₂ cases presented as averaged values.**

169 **4 Discussion**

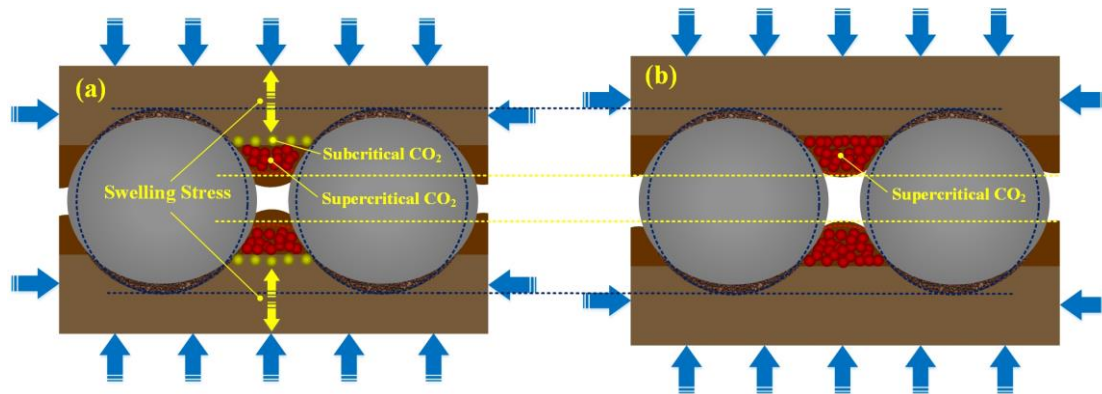
170 The mechanism of permeability evolution in a propped fracture is described schematically in Fig.
 171 6. Different from an intact simple with pores or natural micro-fractures at the nanometer-scale, the
 172 existence of proppant particles (1) provides a macroporous flow channel that is modified by the
 173 synthetic impacts of effective stress, grain embedment and matrix swelling. The gap between grains
 174 (2) generates a pair of non-contacting surfaces, through which swelling magnifies the resulting
 175 fracture closure. The surface deformation of the fracture and the crushed zone between matrix and
 176 grains (3) increases the contact area with permeants and enhances the sorbing capacity. In addition,
 177 the mineral matter tends to be enriched in the crushed zone, which enhances permeant diffusion and
 178 sorption kinetics (Spears & Booth, 2002).



179
180 **Fig. 6. Schematic of flow mechanisms of a propped fracture in shale.**

181 **4.1 Influence of CO₂ phase transition**

182 Permeability decreases precipitously at the beginning of phase transitions from gaseous to both
183 liquid and supercritical states (Fig. 5). However, the influencing mechanisms may be different
184 between these liquid and supercritical transitions – suggested by the differences in the subsequent
185 permeability trends at high pressure. The permeation of liquid CO₂ remains continuous for the
186 overlapping pressure from 7–9 MPa (Group 1 L-CO₂ in Fig. 5). In contrast, the permeability to
187 supercritical CO₂ (SC-CO₂) emerges as a direct climb back to the subcritical level. The liquid case is
188 explained by the sudden volume change during the phase transition for a relatively stable pressure (X.
189 Li et al., 2017). For the supercritical case, the effective aperture variation may be controlled by
190 adsorbed mass and effective stress, graphically described in Fig. 7.



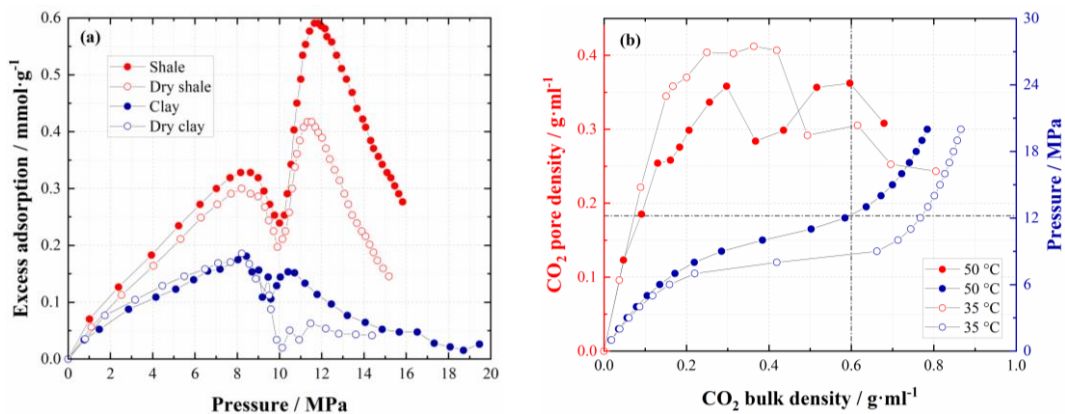
191
192 **Fig. 7. Schematics of effective aperture evolution (a) during the phase transition and (b) under supercritical state.**

193 The phase change of CO₂ near the critical point results in a sharp increase in adsorbed phase
194 density and its resultant swelling strain (Bakhshian & Hosseini, 2019), which compresses the effective
195 aperture and induces a drop in permeability, as shown in Fig. 7(a). The severe swelling strain may
196 consume ~80% of the effective aperture (Hou et al., 2020). Swelling stresses of 9.6–24.7 MPa may
197 result upon introduction of CO₂ at 10 MPa and 44°C measured by uniaxial compaction/swelling test
198 on montmorillonite and shale (Zhang et al., 2018). The swelling stress converts into a free-swelling
199 strain enabled by the non-contacting surfaces (Fig. 6). With increasing swelling, the cumulative stress
200 opposes and overcomes the confining pressure then partly releases the confining-stress-compressed
201 aperture (Fig. 7 (b)) - increasing permeability at the conclusion of the phase transition. The presence
202 of an artificial fracture and grains liberates the swelling stress opposing the confining pressure, which

203 is the essential difference with the intact sample that retains the swelling stress within the rock
 204 structure (Zhi et al., 2019).

205 4.2 Dual-U-shaped evolution due to secondary adsorption in clay

206 Similar concave-upwards evolutions of permeability are present in Parts I and III of the response
 207 which may result from secondary adsorption of CO₂. Direct evidence is reported in studies of CO₂-
 208 clay interactions. The isotherms show dual-inverted-parabolic fluctuations at pressures above ~8–12
 209 MPa in Muderong shale at the same temperature of 45°C. This is attributed to CO₂ adsorption in clay
 210 because of the consistent pattern with the isotherm of pure clay (Kaolinite), as shown in Fig. 8 (a)
 211 (Busch et al., 2008). At micropore scale, the CO₂ pore density (sum of the bulk fluid density and pore
 212 volume normalized excess density) in the clay (montmorillonite) pore is estimated by combining the
 213 data for excess sorption and interlayer thickness measurements. A similar evolution curve is observed
 214 in Fig. 8(b), which is induced by the entrance of supercritical CO₂ into the inter-molecular layer space
 215 within the clay and multilayer sorption at higher fluid density (Rother et al., 2013). More evidence is
 216 apparent in experiments on Texas and Wyoming clays (Romanov, 2013) and Utica shale (Sanguinito
 217 et al., 2018).



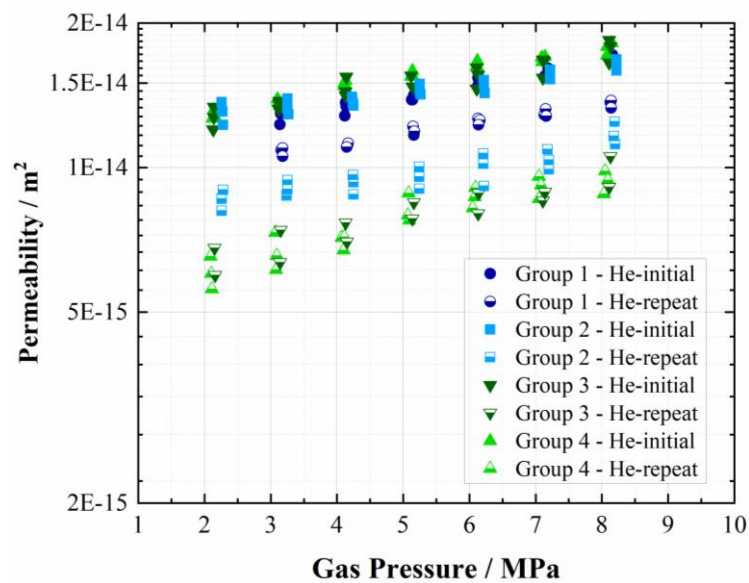
218
 219 **Fig. 8. CO₂ adsorption in shale and clay. (a) Excess adsorption in Muderong shale and kaolinite at 45°C (Busch et**
 220 **al., 2008); (b) CO₂ pore density in montmorillonite as a function of bulk density and corresponding pressure (Rother**
 221 **et al., 2013).**

222 CO₂ adsorption induces swelling strain that consumes the effective aperture in the propped
 223 fracture, thus decreasing permeability with increased swelling. The M-shaped isotherms of CO₂ in
 224 clay (Fig. 8) are the inverse (reflection) of the dual-U-shaped permeability curves (Fig. 5). The
 225 pressures corresponding to the second peak values of adsorption and CO₂ pore density are 11.7 MPa

226 and 12.2 MPa, respectively, which agree with the pressure (11–12 MPa) corresponding to the trough
 227 in the second valley in permeability magnitude in Part III. The previous study of real-time X-ray CT
 228 analysis indicates that clay- and inertite-rich micro-lithotypes hold most of the CO₂ adsorption
 229 increment with increasing gas pressure because of their high porosity (Karacan & Mitchell, 2003). It
 230 may infer that the CO₂ adsorption in clay dominates the secondary permeability evolution.

231 4.3 Generation of secondary adsorption and impact on permeability recovery

232 The difference in response both with (Group 1 and 2) and without (Group 3 and 4) the secondary
 233 adsorption (Part III) is reflected in the permeability recovery between initial and repeat He cases, as
 234 shown in Fig. 9. The permeation of CO₂ swells and softens the rock matrix, which intensifies the
 235 irreversible embedment of grains then restrains the permeability recovery ratio (Hou et al., 2020).
 236 Only ~52% of the permeability, on average, recovers in Groups 3 and 4. For Groups 1 and 2, the
 237 secondary adsorption of supercritical CO₂ could prompt increased embedment that should have
 238 reduced the permeability recovery. In contrast, it raises the permeability to ~79% and ~68% in Groups
 239 1 and 2, respectively.



240
 241 **Fig. 9. Permeability recovery of non-sorbing He both before (initial) and then after (repeat) the injection of**
 242 **sorbing CO₂.**

243 The mechanism of secondary adsorption may result in such abnormal phenomena. The phase
 244 transition of CO₂ into a supercritical state increases the binding energy, which may break the balance
 245 of competitive adsorption between CO₂ and H₂O then dehydrate the clay or other water-containing

246 constituents (Bowers et al., 2017). The macropore flow-channel (Fig. 6) aids this effusion of fugitive
 247 water. The sorption site occupied by a water molecule vacates enough space for 2.2 CO₂ molecules
 248 (Gensterblum, Busch, & Krooss, 2014). Besides, the increasing density of supercritical CO₂ generates
 249 more molecular layers attaching to the surface, thus enhancing the total absorbed mass (Klewiah et
 250 al., 2020; Rother et al., 2013). The higher diffusibility of supercritical CO₂ also increases the
 251 interaction surfaces by diffusing into more pores and deeper into the matrix (S. Li, Li, & Dong, 2016;
 252 Lv, Chi, Zhao, Zhang, & Mu, 2019). Therefore, increasing sorption sites, enabling sorption of multi-
 253 layered molecules and increased diffusion rate of supercritical CO₂ may all contribute to secondary-
 254 adsorption (Fig. 5).

255 Subsequently, the dehydration induces shrinkage of the rock matrix and increases the effective
 256 aperture that follows a cubic law with permeability (Elsworth & Goodman, 1986; Piggott & Elsworth,
 257 1993). Moreover, the dissolution of minerals resulting from the co-existence of CO₂ in water may
 258 additionally enlarge the effective aperture (Weniger, Kalkreuth, Busch, & Krooss, 2010), particularly
 259 for the Green River shale with a high content of carbonates (Dolomite 39.4% and Calcite 12.4%)
 260 (Fang, Elsworth, Wang, Ishibashi, & Fitts, 2017). This may further explain the different recovery
 261 ratios between Group 1 and 2 experiments, where the longer CO₂ exposure leads to greater carbonate
 262 dissolution and higher permeability recovery for Group 1. The irreversible shrinkage and dissolution
 263 enlargement after the desorption of CO₂ in the repeat-He case may contribute to the abnormal
 264 increment of permeability recovery.

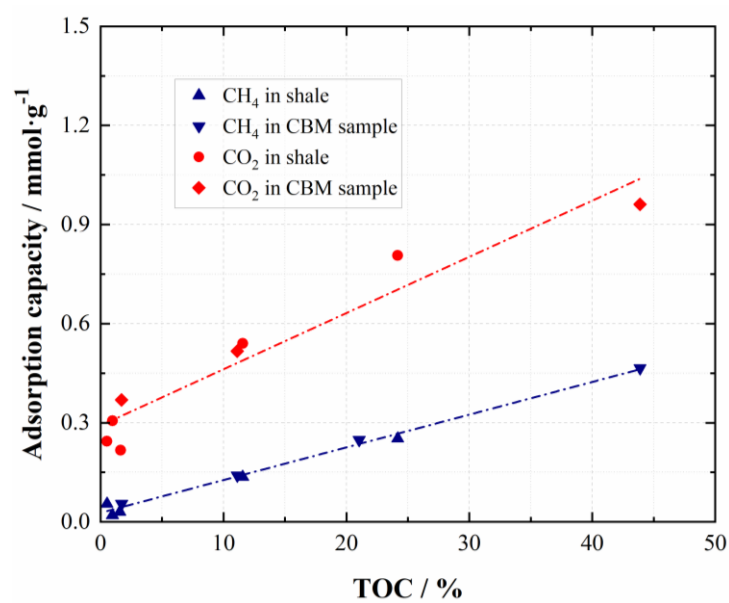
265 **4.4 Contributions of organic and inorganic adsorptions to permeability evolution**

266 The contributions of organic and inorganic adsorptions to the dual-U-shaped permeability
 267 evolution are estimated based on assumptions that (1) the permeability is a sum of functions of
 268 organic adsorption- $f(Org_{ads})$, inorganic adsorption- $f(Inorg_{ads})$ and effective stress- $f'(Effective\ Stress)$,
 269 in which (2) the adsorption functions ($f(Org_{ads}), f(Inorg_{ads})$) are inversely proportional to adsorption
 270 masses. According to assumption (1), the permeability of the adsorptive permeant may be calculated
 271 from

$$\begin{aligned}
 272 \quad Perm &= f(Org_{ads}, Inorg_{ads}, Effective\ Stress) \\
 &= af(Org_{ads}) + bf(Inorg_{ads}) + cf'(Effective\ Stress)
 \end{aligned}
 \tag{3}$$

273 where Org_{ads} and $Inorg_{ads}$ are the adsorption masses of the permeant in the organic and inorganic
 274 constituents, respectively. a , b and c are coefficients and all assigned the value of 1 in this study.

275 The permeability evolution of CH_4 in Green River shale is utilized for a comparative analysis since
 276 the adsorption occurs mainly in the organics, as shown in Fig. 10 (Weniger et al., 2010). As the TOC
 277 content reduces, the CH_4 adsorption in shale approaches zero and yet residual CO_2 adsorption remains
 278 in the inorganic constituents under the same condition. Similar results are reported in experiments on
 279 shales from the United States (Matus Gasparik et al., 2014) and South China (Tan et al., 2014). The
 280 maximum sorption capacity of CH_4 commonly appears at a lower pressure than that of CO_2 , even in
 281 the same shale. Langmuir pressures to CO_2 and CH_4 in a group of split tests are approximately a factor
 282 of two different (Table 2). The corresponding pressures of the minimum permeability in Part III (11–
 283 12MPa) and I (5–6MPa) are also offset by a factor of two, as shown in Fig. 5.



284 Fig. 10. Adsorption capacities of CH_4 and CO_2 versus TOC (in shale and CBM sample, 45°C and ~12 MPa)
 285 (Weniger et al., 2010).
 286

287 Table 2. Comparison of Langmuir pressure (P_L) between CO_2 and CH_4 in shale samples from Paraná Basin,
 288 Brazil (Weniger et al., 2010)

No.	Rock Type	$n_L CH_4$ mmol/g	$P_L CH_4$ MPa	$n_L CO_2$ mmol/g	$P_L CO_2$ MPa	P_{LCO_2} / P_{LCH_4}
07_114	Carbonate Shale	0.07	4.09	0.69	8.43	2.06
07_117/118		0.28	2.31	0.8	6.19	2.68
07_181		0.18	5.79	0.9	12.01	2.07
08_100	Shale	0.04	16.09	0.78	20	1.24
08_101		0.08	7.09	0.69	19.03	2.68
08_168		0.37	8.39	2.02	15	1.79
08_170		0.25	14.16	1.25	13.43	0.95
08_154		0.04	5.65	0.65	19.9	3.52

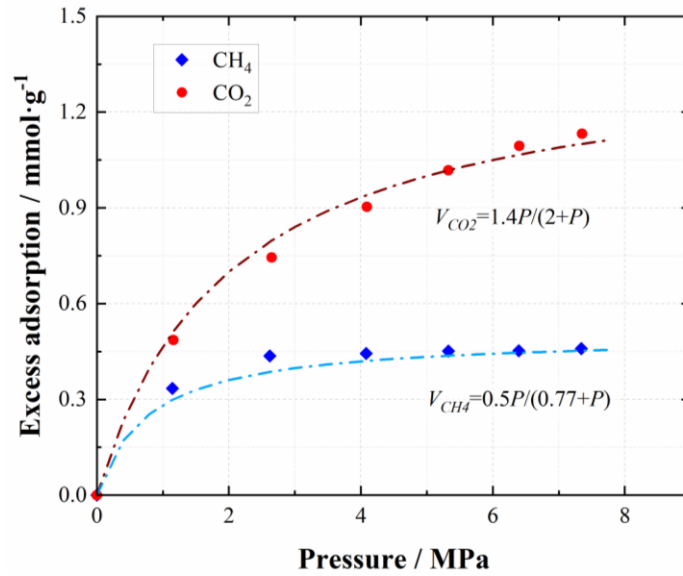
289
290

Based on assumption (2), the contribution ratio of CO₂ and CH₄ adsorption to permeability in

291 organics in the same sample is expressed as

$$292 \quad \frac{f(Org_{ads})_{CO_2}}{f(Org_{ads})_{CH_4}} = \frac{f(Adsorption\ Mass_{CO_2})}{f(Adsorption\ Mass_{CH_4})} = \frac{Adsorption\ Mass_{CH_4}}{Adsorption\ Mass_{CO_2}} \quad (4)$$

293 The adsorption masses under various pressures are estimated by the Langmuir model, in which the
294 maximum adsorption volume and Langmuir pressure are fitted using the measurements in anthracite
295 for its high carbon content (>90%), as shown in Fig. 11 (Merkel, Gensterblum, Krooss, & Amann,
296 2015).



297

298 Fig. 11. Excess adsorption (45°C) of CH₄ and CO₂ in anthracite and fitted Langmuir equations (Merkel et al., 2015).

299 Eq. (4) is then resolved as

$$300 \quad \frac{f(Org_{ads})_{CO_2}}{f(Org_{ads})_{CH_4}} = \frac{Adsorption\ Mass_{CH_4}}{Adsorption\ Mass_{CO_2}} = \frac{5}{14} \frac{2 + P}{0.77 + P} \quad (5)$$

301 where P is the injection pressure, MPa.

302 The ratio of permeabilities under the same effective pressure in the same sample is calculated as

$$303 \quad \frac{Perm_{CO_2}}{Perm_{He}} = \frac{f(Org_{ads})_{CO_2} + f(Inorg_{ads})_{CO_2} + f'(Effective\ Stress)}{f'(Effective\ Stress)} \quad (6)$$

304 and

$$305 \quad \frac{Perm_{CH_4}}{Perm_{He}} = \frac{f(Org_{ads})_{CH_4} + f'(Effective\ Stress)}{f'(Effective\ Stress)} \quad (7)$$

306 where the adsorption of CH₄ in inorganics is ignored comparing with that of CO₂ (Fig. 10).
 307 The normalization of Eqs. (6) and (7) relative to effective stress is applied to eliminate this effect in
 308 their intercomparisons. Then,

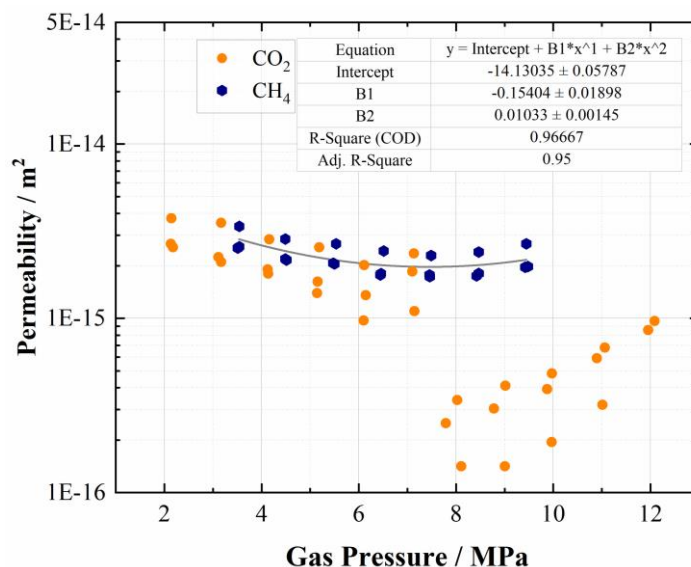
$$309 \quad \frac{f(Org_{ads})_{CH_4}}{f(Org_{ads})_{CO_2} + f(Inorg_{ads})_{CO_2}} = \frac{Perm_{CH_4} / Perm_{He} - 1}{Perm_{CO_2} / Perm_{He} - 1} \quad (8)$$

310 We define the relative contribution of organic and inorganic adsorption to permeability evolution for
 311 the case of CO₂ as “Contribution ratio”. Combing Eqs. (5) and (8), it is estimated as

$$312 \quad Contribution\ ratio_{Org_{ads}} = \frac{f(Org_{ads})_{CO_2}}{f(Org_{ads})_{CO_2} + f(Inorg_{ads})_{CO_2}} = \frac{5}{14} \frac{2 + P}{0.77 + P} \frac{Perm_{CH_4} / Perm_{He} - 1}{Perm_{CO_2} / Perm_{He} - 1} \quad (9)$$

$$313 \quad Contribution\ ratio_{Inorg_{ads}} = 1 - Contribution\ rate_{Org_{ads}} \quad (10)$$

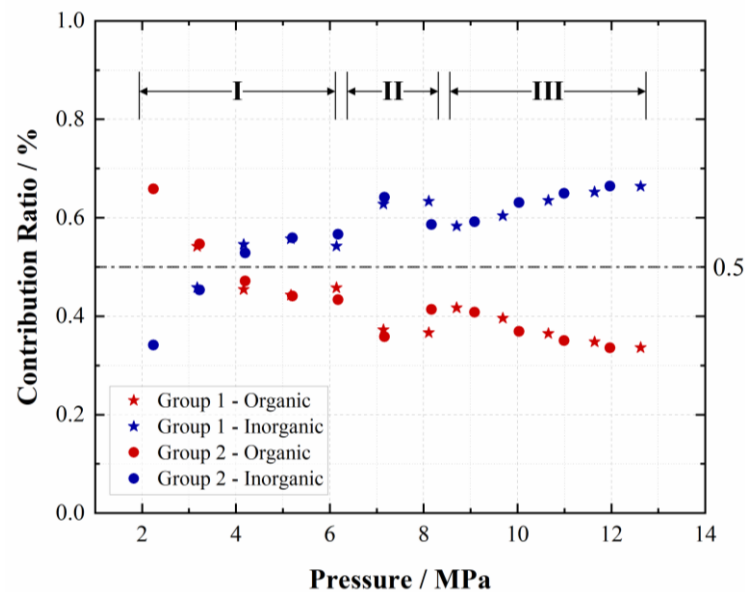
314 The averaged data from Groups 1 and 2 (Fig. 4), excluding the liquid CO₂ and He-repeat cases, are
 315 employed to define the permeabilities to CO₂ and He. The permeability to CH₄ is recovered from
 316 measurements using the same material (Green River shale and 40/80 Carbo-Lite proppant) and similar
 317 apparatus and procedures, as shown in Fig. 12 (X. Li et al., 2017). The approximations for CO₂
 318 permeability are reported and compared with those in Fig. 4.



319
 320 **Fig. 12. Permeability evolution in Green River shale upon injection of CO₂ and CH₄ at a temperature of 21°C and**
 321 **confining pressure of 20 MPa (X. Li et al., 2017).**

322 The ratios of the contribution of organic and inorganic adsorption to permeability evolution are
 323 analyzed by Eqs. (9) and (10) and plotted in Fig. 13. A flat X-shaped curve is presented, in which the
 324 contribution of adsorption to the organic fraction decreases with increasing pressure, while the

325 inorganic contribution increases with increasing pressure. Reflected in the tripartite permeability
 326 evolution, the effect of organic adsorption is initially dominant but decreases rapidly before flattening
 327 out in Part I. The effect of inorganic adsorption increases with increasing pressure before approaching
 328 the magnitude of the effect to that of organic adsorption under subcritical pressure. For the secondary
 329 adsorption of Part III, the inorganic constituents (mainly clay with high porosity and high surface
 330 area) provide most of the sorption sites and contribute 60–70% of the total adsorptive fractions that
 331 induce another U-shaped evolution of permeability under supercritical conditions. Similarly, the
 332 previous study of real-time X-ray CT scanning on the different positions of a coal sample shows that
 333 the vitrinite-liptinite-region and clay-inertinite-region adsorbed 19% and 81% of CO₂ (4.42 MPa),
 334 respectively (Karacan & Mitchell, 2003).



335
 336 **Fig. 13. Relative contribution ratio of organic and inorganic adsorptions to permeability evolution for supercritical**
 337 **CO₂ (45°C) in the propped shale fracture.**

338 5 Conclusions

339 Permeability evolution in propped shale fractures to non-adsorptive He and adsorptive CO₂ have
 340 been measured across both sub- and super-critical conditions. The CO₂-matrix and grain-to-surface
 341 interactions, CO₂ phase transition and their mutual effects are analysed to reveal mechanisms of
 342 permeability evolution. Contributions of CO₂ adsorption to permeability evolution are classified and
 343 quantified by comparing with responses to slightly-adsorptive CH₄ and non-adsorptive He. The main
 344 observations of this work are as follow:

345 (1) A tripartite permeability curve is apparent for supercritical CO₂, including dual-U-shaped
346 evolutions at pressures first below (I) and then exceeding (III) the critical point (pressure) with a
347 precipitous V-shaped fluctuation during the intervening case of the phase transition (II). Different
348 from the case of subcritical CO₂, the initial permeability drop at the beginning of the phase transition
349 may be induced by an increase in the adsorbed-phase-density and the resulting swelling strain. The
350 subsequent recovery of permeability may result from the accumulative swelling stress that overcomes
351 the confining pressure and partly releases the confining-stress-compressed aperture.

352 (2) The dual-U-shaped permeability evolution is controlled by CO₂ adsorptions. The phase
353 transition of CO₂ may increase the binding energy that favors its competitive adsorption with H₂O and
354 results in more sorption sites. Additionally, an increased diffusivity and density of supercritical CO₂
355 increases the interaction surface area and generates multilayer molecular sorption onto the surface,
356 respectively. These synthetic factors result in a secondary-adsorption then a secondary-U-shaped
357 permeability evolution at fluid pressures in excess of the critical condition.

358 (3) The abnormal increments of permeability recovery for He-repeat cases in Groups 1 and 2 are
359 observed where secondary-adsorption occurs. Dehydration by the competitive adsorption between
360 CO₂ and H₂O shrinks the matrix, especially for the clay constituents. The accompanying process of
361 mineral dissolution by the co-existence of CO₂ in water makes an extra contribution. Irreversible
362 matrix shrinkage and mineral dissolution yield larger effective aperture that results in abnormal
363 increments of permeability recovery after the desorption of CO₂.

364 (4) Mechanisms of permeability evolution for CO₂ in shale are classified between organic and
365 inorganic fractions. Each contribution to the permeability evolution is quantified by comparison
366 between CH₄ and He measurements. A flat X-shaped trend is apparent, in which the inorganic
367 contribution increases rapidly with increasing pressure then flattens out while the organic contribution
368 decreases rapidly with increasing pressure then levels off. The inorganic constituents (mainly clay
369 with high porosity and large surface area) provide most of the sorption sites and contribute 60–70% of
370 the total adsorptive fractions that result in the secondary-U-shaped permeability evolution under
371 supercritical conditions.

372

373

374 **Acknowledgements**



375

376 This research has received funding from the European Union's Horizon 2020 research and
377 innovation programme under the Marie Skłodowska-Curie grant agreement No 846775.

378 **References**

- 379 Akono, A. T., Druhan, J. L., Davila, G., Tsotsis, T., Jessen, K., Fuchs, S., . . . Werth, C. J. (2019). A
380 review of geochemical-mechanical impacts in geological carbon storage reservoirs.
381 *Greenhouse Gases-Science and Technology*, 9(3), 474-504. doi:10.1002/ghg.1870
- 382 Ao, X., Lu, Y., Tang, J., Chen, Y., & Li, H. (2017). Investigation on the physics structure and
383 chemical properties of the shale treated by supercritical CO₂. *Journal of CO₂ Utilization*, 20,
384 274-281. doi:10.1016/j.jcou.2017.05.028
- 385 Arshadi, M., Zolfaghari, A., Piri, M., Al-Muntasheri, G. A., & Sayed, M. (2017). The effect of
386 deformation on two-phase flow through proppant-packed fractured shale samples: A micro-
387 scale experimental investigation. *Advances in Water Resources*, 105, 108-131.
388 doi:10.1016/j.advwatres.2017.04.022
- 389 Bakhshian, S., & Hosseini, S. A. (2019). Prediction of CO₂ adsorption-induced deformation in shale
390 nanopores. *Fuel*, 241, 767-776. doi:10.1016/j.fuel.2018.12.095
- 391 Bielicki, J. M., Langenfeld, J. K., Tao, Z., Middleton, R. S., Menefee, A. H., & Clarens, A. F. (2018).
392 The geospatial and economic viability of CO₂ storage in hydrocarbon depleted fractured
393 shale formations. *International Journal of Greenhouse Gas Control*, 75, 8-23.
394 doi:10.1016/j.ijggc.2018.05.015
- 395 Bowers, G. M., Schaef, H. T., Loring, J. S., Hoyt, D. W., Burton, S. D., Walter, E. D., & Kirkpatrick,
396 R. J. (2017). Role of Cations in CO₂ Adsorption, Dynamics, and Hydration in Smectite Clays
397 under in Situ Supercritical CO₂ Conditions. *The Journal of Physical Chemistry C*, 121(1),
398 577-592. doi:10.1021/acs.jpcc.6b11542
- 399 Brace, W. F., Walsh, J. B., & Frangos, W. T. (1968). Permeability of granite under high pressure.
400 *Journal of Geophysical Research*, 73(6), 2225-2236. doi:10.1029/JB073i006p02225
- 401 Busch, A., Alles, S., Gensterblum, Y., Prinz, D., Dewhurst, D., Raven, M., . . . Krooss, B. (2008).
402 Carbon dioxide storage potential of shales. *International Journal of Greenhouse Gas Control*,
403 2(3), 297-308. doi:10.1016/j.ijggc.2008.03.003
- 404 Buscheck, T. A., White, J. A., Carroll, S. A., Bielicki, J. M., & Aines, R. D. (2016). Managing
405 geologic CO₂ storage with pre-injection brine production: a strategy evaluated with a model

406 of CO2 injection at Snøhvit. *Energy & Environmental Science*, 9(4), 1504-1512.
407 doi:10.1039/c5ee03648h

408 Cao, M., & Gu, Y. (2013). Oil recovery mechanisms and asphaltene precipitation phenomenon in
409 immiscible and miscible CO2 flooding processes. *Fuel*, 109, 157-166.
410 doi:10.1016/j.fuel.2013.01.018

411 Chalmers, G. R. L., & Bustin, R. M. (2008). Lower Cretaceous gas shales in northeastern British
412 Columbia, Part I: geological controls on methane sorption capacity. *Bulletin of Canadian
413 Petroleum Geology*, 56(1), 1-21. doi:10.2113/gscpgbull.56.1.1

414 Elsworth, D., & Goodman, R. E. (1986). Characterization of rock fissure hydraulic conductivity using
415 idealized wall roughness profiles. *International Journal of Rock Mechanics and Mining
416 Sciences & Geomechanics Abstracts*, 23(3), 233-243.

417 Fang, Y., Elsworth, D., Wang, C., Ishibashi, T., & Fitts, J. P. (2017). Frictional stability-permeability
418 relationships for fractures in shales. *Journal of Geophysical Research: Solid Earth*, 122(3),
419 1760-1776. doi:10.1002/2016jb013435

420 Gale, J. F. W., Laubach, S. E., Olson, J. E., Eichhuble, P., & Fall, A. (2014). Natural Fractures in
421 shale: A review and new observations. *AAPG Bulletin*, 98(11), 2165-2216.
422 doi:10.1306/08121413151

423 Gasparik, M., Bertier, P., Gensterblum, Y., Ghanizadeh, A., Krooss, B. M., & Littke, R. (2014).
424 Geological controls on the methane storage capacity in organic-rich shales. *International
425 Journal of Coal Geology*, 123, 34-51. doi:10.1016/j.coal.2013.06.010

426 Gasparik, M., Ghanizadeh, A., Bertier, P., Gensterblum, Y., Bouw, S., & Krooss, B. M. (2012). High-
427 Pressure Methane Sorption Isotherms of Black Shales from The Netherlands. *Energy &
428 Fuels*, 26(8), 4995-5004. doi:10.1021/ef300405g

429 Gensterblum, Y., Busch, A., & Krooss, B. M. (2014). Molecular concept and experimental evidence
430 of competitive adsorption of H2O, CO2 and CH4 on organic material. *Fuel*, 115, 581-588.
431 doi:10.1016/j.fuel.2013.07.014

432 Hoek, E., & Martin, C. D. (2014). Fracture initiation and propagation in intact rock – A review.
433 *Journal of Rock Mechanics and Geotechnical Engineering*, 6(4), 287-300.
434 doi:10.1016/j.jrmge.2014.06.001

435 Hou, L., Elsworth, D., & Geng, X. (2020). Swelling and embedment induced by sub- and super-
436 critical-CO₂ on the permeability of propped fractures in shale. *International Journal of Coal*
437 *Geology*. doi:10.1016/j.coal.2020.103496

438 Hou, L., Jiang, T., Liu, H., Geng, X., Sun, B., Li, G., & Meng, S. (2017). An evaluation method of
439 supercritical CO₂ thickening result for particle transporting. *Journal of CO₂ Utilization*, 21,
440 247-252. doi:10.1016/j.jcou.2017.07.023

441 Jia, B., Tsau, J.-S., & Barati, R. (2018). Different Flow Behaviors of Low-Pressure and High-Pressure
442 Carbon Dioxide in Shales. *SPE Journal*, 23(04), 1452-1468. doi:10.2118/191121-pa

443 Karacan, C. Ö., & Mitchell, G. D. (2003). Behavior and effect of different coal microlithotypes during
444 gas transport for carbon dioxide sequestration into coal seams. *International Journal of Coal*
445 *Geology*, 53(4), 201-217. doi:10.1016/s0166-5162(03)00030-2

446 Kewen Li, Y. G., Youchang Lyu. (2015). New mathematical models for calculating proppant
447 embedment and fracture conductivity. *SPE Journal*, 20(03), 1-12.

448 Klewiah, I., Berawala, D. S., Alexander Walker, H. C., Andersen, P. Ø., & Nadeau, P. H. (2020).
449 Review of experimental sorption studies of CO₂ and CH₄ in shales. *Journal of Natural Gas*
450 *Science and Engineering*, 73. doi:10.1016/j.jngse.2019.103045

451 Kumar, H., Elsworth, D., Liu, J., Pone, D., & Mathews, J. P. (2015). Permeability evolution of
452 propped artificial fractures in coal on injection of CO₂. *Journal of Petroleum Science and*
453 *Engineering*, 133, 695-704. doi:10.1016/j.petrol.2015.07.008

454 Lan, Y., Yang, Z., Wang, P., Yan, Y., Zhang, L., & Ran, J. (2019). A review of microscopic seepage
455 mechanism for shale gas extracted by supercritical CO₂ flooding. *Fuel*, 238, 412-424.
456 doi:10.1016/j.fuel.2018.10.130

457 Li, S., Li, Z., & Dong, Q. (2016). Diffusion coefficients of supercritical CO₂ in oil-saturated cores
458 under low permeability reservoir conditions. *Journal of CO₂ Utilization*, 14, 47-60.
459 doi:10.1016/j.jcou.2016.02.002

460 Li, X., Feng, Z., Han, G., Elsworth, D., Marone, C., Saffer, D., & Cheon, D.-S. (2017). Permeability
461 Evolution of Propped Artificial Fractures in Green River Shale. *Rock Mechanics and Rock*
462 *Engineering*, 50(6), 1473-1485. doi:10.1007/s00603-017-1186-2

463 Lu, Y., Ao, X., Tang, J., Jia, Y., Zhang, X., & Chen, Y. (2016). Swelling of shale in supercritical
464 carbon dioxide. *Journal of Natural Gas Science and Engineering*, 30, 268-275.
465 doi:10.1016/j.jngse.2016.02.011

466 Luo, X., Wang, S., Wang, Z., Jing, Z., Lv, M., Zhai, Z., & Han, T. (2015). Adsorption of methane,
467 carbon dioxide and their binary mixtures on Jurassic shale from the Qaidam Basin in China.
468 *International Journal of Coal Geology*, 150-151, 210-223. doi:10.1016/j.coal.2015.09.004

469 Lv, J., Chi, Y., Zhao, C., Zhang, Y., & Mu, H. (2019). Experimental study of the supercritical CO₂
470 diffusion coefficient in porous media under reservoir conditions. *R Soc Open Sci*, 6(6),
471 181902. doi:10.1098/rsos.181902

472 Merkel, A., Gensterblum, Y., Krooss, B. M., & Amann, A. (2015). Competitive sorption of CH₄,
473 CO₂ and H₂O on natural coals of different rank. *International Journal of Coal Geology*, 150-
474 151, 181-192. doi:10.1016/j.coal.2015.09.006

475 Middleton, R. S., Carey, J. W., Currier, R. P., Hyman, J. D., Kang, Q., Karra, S., . . . Viswanathan, H.
476 S. (2015). Shale gas and non-aqueous fracturing fluids: Opportunities and challenges for
477 supercritical CO₂. *Applied Energy*, 147, 500-509. doi:10.1016/j.apenergy.2015.03.023

478 Pan, Z., & Connell, L. D. (2007). A theoretical model for gas adsorption-induced coal swelling.
479 *International Journal of Coal Geology*, 69(4), 243-252. doi:10.1016/j.coal.2006.04.006

480 Piggott, A. R., & Elsworth, D. (1993). Laboratory assessment of the equivalent apertures of a rock
481 fracture. *GEOPHYSICAL RESEARCH LETTERS*, 20(13), 1387-1390.

482 Romanov, V. N. (2013). Evidence of irreversible CO₂ intercalation in montmorillonite. *International*
483 *Journal of Greenhouse Gas Control*, 14, 220-226. doi:10.1016/j.ijggc.2013.01.022

484 Rother, G., Ilton, E. S., Wallacher, D., Haubeta, T., Schaef, H. T., Qafoku, O., . . . Bodnar, R. J.
485 (2013). CO₂ sorption to subsingle hydration layer montmorillonite clay studied by excess
486 sorption and neutron diffraction measurements. *Environ Sci Technol*, 47(1), 205-211.
487 doi:10.1021/es301382y

488 Sanguinito, S., Goodman, A., Tkach, M., Kutchko, B., Culp, J., Natesakhawat, S., . . . Crandall, D.
489 (2018). Quantifying dry supercritical CO₂-induced changes of the Utica Shale. *Fuel*, 226, 54-
490 64. doi:10.1016/j.fuel.2018.03.156

491 Spears, D. A., & Booth, C. A. (2002). The composition of size-fractionated pulverised coal and the
492 trace element associations. *Fuel*, 81(5), 683-690. doi:10.1016/s0016-2361(01)00156-9

493 Tan, J., Weniger, P., Krooss, B., Merkel, A., Horsfield, B., Zhang, J., . . . Tocher, B. A. (2014). Shale
494 gas potential of the major marine shale formations in the Upper Yangtze Platform, South
495 China, Part II: Methane sorption capacity. *Fuel*, 129, 204-218. doi:10.1016/j.fuel.2014.03.064

496 Tang, Y., & Ranjith, P. G. (2018). An experimental and analytical study of the effects of shear
497 displacement, fluid type, joint roughness, shear strength, friction angle and dilation angle on
498 proppant embedment development in tight gas sandstone reservoirs. *International Journal of*
499 *Rock Mechanics and Mining Sciences*, 107, 94-109. doi:10.1016/j.ijrmms.2018.03.008

500 Tayari, F., & Blumsack, S. (2020). A real options approach to production and injection timing under
501 uncertainty for CO₂ sequestration in depleted shale gas reservoirs. *Applied Energy*, 263.
502 doi:10.1016/j.apenergy.2020.114491

503 Wang, L., & Yu, Q. (2016). The effect of moisture on the methane adsorption capacity of shales: A
504 study case in the eastern Qaidam Basin in China. *Journal of Hydrology*, 542, 487-505.
505 doi:10.1016/j.jhydrol.2016.09.018

506 Wang, S., Elsworth, D., & Liu, J. (2011). Permeability evolution in fractured coal: The roles of
507 fracture geometry and water-content. *International Journal of Coal Geology*, 87(1), 13-25.
508 doi:10.1016/j.coal.2011.04.009

509 Wang, S., Elsworth, D., & Liu, J. (2013). Permeability evolution during progressive deformation of
510 intact coal and implications for instability in underground coal seams. *International Journal*
511 *of Rock Mechanics and Mining Sciences*, 58, 34-45. doi:10.1016/j.ijrmms.2012.09.005

512 Weng, X. (2015). Modeling of complex hydraulic fractures in naturally fractured formation. *Journal*
513 *of Unconventional Oil and Gas Resources*, 9, 114-135. doi:10.1016/j.juogr.2014.07.001

514 Weniger, P., Kalkreuth, W., Busch, A., & Krooss, B. M. (2010). High-pressure methane and carbon
515 dioxide sorption on coal and shale samples from the Paraná Basin, Brazil. *International*
516 *Journal of Coal Geology*, 84(3-4), 190-205. doi:10.1016/j.coal.2010.08.003

517 Yin, H., Zhou, J., Jiang, Y., Xian, X., & Liu, Q. (2016). Physical and structural changes in shale
518 associated with supercritical CO₂ exposure. *Fuel*, 184, 289-303.
519 doi:10.1016/j.fuel.2016.07.028

520 Yin, H., Zhou, J., Xian, X., Jiang, Y., Lu, Z., Tan, J., & Liu, G. (2017). Experimental study of the
521 effects of sub- and super-critical CO₂ saturation on the mechanical characteristics of organic-
522 rich shales. *Energy*, 132, 84-95. doi:10.1016/j.energy.2017.05.064

523 Zhang, M., de Jong, S. M., Spiers, C. J., Busch, A., & Wentinck, H. M. (2018). Swelling stress
524 development in confined smectite clays through exposure to CO₂. *International Journal of*
525 *Greenhouse Gas Control*, 74, 49-61. doi:10.1016/j.ijggc.2018.04.014

526 Zhi, S., Elsworth, D., & Liu, L. (2019). W-shaped permeability evolution of coal with supercritical
527 CO₂ phase transition. *International Journal of Coal Geology*, 211, 1-14.
528 doi:10.1016/j.coal.2019.103221

529 Zhou, J., Liu, G., Jiang, Y., Xian, X., Liu, Q., Zhang, D., & Tan, J. (2016). Supercritical carbon
530 dioxide fracturing in shale and the coupled effects on the permeability of fractured shale:
531 An experimental study. *Journal of Natural Gas Science and Engineering*, 36, 369-377.
532 doi:10.1016/j.jngse.2016.10.005

533 Zhou, J., Tian, S., Zhou, L., Xian, X., Yang, K., Jiang, Y., . . . Guo, Y. (2020). Experimental
534 investigation on the influence of sub- and super-critical CO₂ saturation time on the
535 permeability of fractured shale. *Energy*, 191. doi:10.1016/j.energy.2019.116574

536